Design and Demonstration of Novel QW Intermixing Scheme for the Integration of UTC-Type Photodiodes With QW-Based Components

James W. Raring, *Student Member, IEEE*, Erik J. Skogen, *Member, IEEE*, Chad S. Wang, *Student Member, IEEE*, Jonathon S. Barton, *Member, IEEE*, Gordon B. Morrison, Stephane Demiguel, *Member, IEEE*, Steven P. DenBaars, *Member, IEEE*, and Larry A. Coldren, *Fellow, IEEE*

***Abstract*—We present the design and demonstration of unitraveling carrier (UTC) photodiodes fabricated using a novel quantum-well (QW) intermixing and metal–organic chemical vapor deposition (MOCVD) regrowth fabrication platform. The photodiodes discussed here were realized on the same chip as high gain centered QW active regions, intermixed passive centered well waveguides, and low optical confinement offset QW active regions regrown over intermixed wells. This demonstration lifts previous constraints imposed on high functionality photonic circuits, which forced a common waveguide architecture in the detector, laser, and amplifier by validating a platform suited for the monolithic integration of UTC photodiodes into photonic integrated circuits comprised of widely tunable high gain laser diodes, high efficiency modulators, and low optical confinement high saturation power semiconductor optical amplifiers. In this manuscript we focus on the design and performance of UTC photodiodes fabricated on intermixed QWs using this novel scheme. The photodiodes exhibit ~90% internal quantum efficiency, excellent photocurrent handling capabilities, and minimal response roll-off over the 20 GHz of our testing capability. The 40 Gb/s operation was achieved with the demonstration of open eye diagrams.**

***Index Terms*—Electro-absorption modulators, metal–organic chemical vapor deposition (MOCVD), monolithic integration, quantum-well intermixing (QWI), semiconductor lasers, semiconductor optical amplifier (SOA), unitraveling carrier (UTC) photodiodes.**

I. Introduction

A. Photodiodes

FUNCTIONING to convert signals from the optical to the electrical domain, photodiodes are the core element of optical receivers and are thus key components in optical networks. In conventional receivers, the photodetector is followed by a transimpedence electrical amplifier for signal amplification. The sensitivity of this configuration is limited by the front-end noise of the electrical amplifier. The emergence of fiber amplifiers and the development of semiconductor amplifiers for pre-detection amplification has enabled the realization of significantly higher signal-to-noise ratios [1]. In this configuration, the demands on the photodetector are drastically increased since they are forced to handle the higher photocurrents generated in the detectors with the larger incident optical powers. It is essential that the detectors maintain high speed and high efficiency operation at high power levels.

High-speed high-efficiency p-i-n photodiodes have been developed with the use of a side illuminated waveguide structure and traveling wave electrodes [2]. However, the photocurrent handling capabilities of this type of photodetector is intrinsically limited for two reasons. Saturation in a p-i-n photodetector can be explained by the classic space charge effect, which is a result of the slow escape time of holes from the absorbing layer. The spatial distribution of photogenerated carriers in the absorbing medium effectively reduces the applied electric field due to screening effects. Once the field drops below a critical value, the holes can no longer maintain their saturation velocity and the power in versus power out response of the device begins to roll-off. The second source of low saturation current densities in side-illuminated p-i-n detectors is the nonuniform generation of carriers along the length of the detector. The exponential absorption profile leads to significantly greater current densities at the front-end of the diode, and thus degrades the overall performance of the detector. However, this front-end saturation can be greatly reduced without altering the internal physics within the photodetector by evanescently coupling the optical power from the core waveguide into the absorbing layer [2].

The unitraveling carrier (UTC) photodiode has been designed specifically to circumvent the influence of hole transport on the performance of the detector by making the total charge transit time heavily dominated by electrons. The theory outlined in [3] offers an expression for carrier transport times entirely governed by electrons. Since the overshoot velocity of electrons is an order of magnitude higher than the saturation velocity of holes, the UTC can achieve saturation current densities four to six times higher than that in p-i-n photodiodes [3]. Due to the superior photocurrent handling capabilities, the UTC photodiode has received a great deal of recent attention. The theory of operation and demonstration of such photodiodes have been extensively reported [3], [4]. As the technology has matured over

Manuscript received June 28, 2005; revised September 19, 2005.

J. W. Raring, C. S. Wang, J. S. Barton, and S. P. DenBaars are with the Materials Department, University of California, Santa Barbara, CA 93106 USA (e-mail: jraring@engineering.ucsb.edu; cswang@engineering.ucsb.edu; jsbarton@engineering.ucsb.edu; denbaars@engineering.ucsb.edu).

E. J. Skogen is with the Sandia National Laboratories, Albuquerque, NM 87123 USA (e-mail: ejskoge@sandia.gov).

G. B. Morrison is with ThreeFive Photonics, 3994 DB Houten, The Netherlands.

S. Demiguel is with the University of Texas at Austin, Austin, TX 78758 USA (e-mail: stephane_demiguel@yahoo.com).

L. A. Coldren are with the Electrical and Computer Engineering Department, University of California, Santa Barbara, CA 93106 USA (e-mail: tallest_dwarf@hotmail.com; coldren@ece.ucsb.edu).

Digital Object Identifier 10.1109/JQE.2005.862030

0018-9197/$20.00 © 2006 IEEE

the past several years, further advances have been made such as charge compensated UTCs and most recently, nearly ballistic UTCs [4], [5]. To the best of our knowledge, there have been no reports presenting a UTC photodiode fabricated using an integration platform specifically designed for extremely high functionality monolithic integration. Previous reports have focused on discrete UTC photodiodes or photodiodes integrated with one other active component such as a modulator [6].

B. Monolithic Integration

Monolithic integration of photonic circuits offers tremendous advantages in optical network applications such as high functionality, improved efficiency, decreased size, and lower costs. As the functionality demands on photonic integrated circuits (PIC) continues to increase, the circuits will inevitably require higher levels of integration complexity. With this complexity, the realization of an optimally performing device becomes a far more arduous task due to the design constraints often imposed by monolithic integration.

There are several examples of high functionality PICs in which a photodiode must be monolithically integrated with other active components such as semiconductor optical amplifiers (SOA), the widely tunable sampled-grating DBR laser (SG-DBR), and quantum-well (QW) electroabsorption modulators (EAM). Photocurrent-driven wavelength converters (PD-WC) and transceivers are two such examples, as these devices will facilitate enabling technologies such as dynamic provisioning and wavelength routing [7].

The PD-WC is a particularly challenging device since the individual components necessitate unique waveguide architectures for optimum performance. Low threshold, high efficiency lasers require high optical confinement QW active region architecture for maximized modal gain. Integrated QW EAMs necessitate a QW band-edge that is blue-shifted from that of the laser or SOA operation wavelength for reasonable insertion loss/extinction properties. State of the art SOA's employ a low optical confinement QW active region architecture such that the photon density over the active QWs can be kept low and high saturation powers can be achieved [8]. Finally, as discussed above, a photodiode designed for high photocurrent/high speed operation should employ a unique internal structure such as the UTC-type photodiode, which mitigates the saturation effects induced by hole transport and/or employs a waveguide architecture designed to minimize front-end saturation.

Conventional fabrication schemes offer little flexibility in the cross-sectional waveguide architectures within the individual components of highly complex devices such as single-chip PD-WCs. This has resulted in individual components sharing the same waveguide architecture such as a common QW stack in the laser, SOA, and photodetector, ultimately limiting the device performance as reported in [9]. Thus, a key challenge of the PIC designer has been to allocate the tradeoffs in such a way that the overall performance of the device is sufficient for the intended application.

C. Integration Technology

With the growing performance demands and increasing data rates of PICs, the design space will be exhausted on conventional integration platforms and next generation platforms will be essential. Various methods for manipulating the material properties to achieve multiple QW band edges within a single PIC have been reported such as butt-joint growth, selective area growth (SAG), and QW intermixing (QWI) [10]–[12]. In the butt-joint scheme, the optical waveguide is selectively removed in regions where a different band-edge material or alternative waveguide structure is desired. This is followed by a nonplanar regrowth in which the alternative desired material is deposited. The difficulty with this scheme resides in the high degree of thickness and material composition matching required at the waveguide interfaces such that reflections and loss are minimized [10]. In SAG, a carefully designed dielectric mask is defined on the sample prior to growth such that the growth rate and hence the QW band-edge adjacent to the mask is controlled. Since this technique exploits the contrast in surface kinetics of the growth constituents on the semiconductor and dielectric, a high degree of calibration/optimization is required to tightly control the reactor conditions. The abruptness of the transition regions is limited by the surface diffusion length of the growth constituents, which may be on the order of tens of microns. Additionally, the optical mode overlap with the mulitple QW (MQW) may not be ideal in all sections due to the thickness variation [11].

Here we use a simple and robust QWI method to precisely control the QW band-edge orthogonal to the growth direction without any disruption of the waveguide in the axial direction. In the QWI process detailed in [12], point defects are created by ion implantation into an InP buffer layer over the MQW active region. During a high temperature anneal, the point defects are diffused through the MQW region, promoting the interdiffusion of group V-atoms between the wells and barriers. The interdiffusion reshapes the QW profile by distorting the QW–barrier interface. The result is a shift in the quantized energy levels in the well, and hence a shift in the band edge energy. Following the QWI process, we use MOCVD regrowth to realize unique waveguide architectures such as low optical confinement QW active regions and UTC photodiode structures. The blanket regrowth performed here is relatively straightforward and does not require the additional growth precision necessary for butt-joint growth or sample patterning in SAG [13].

In previous work, we have demonstrated viable 10 Gb/s, high efficiency, negative-chirp, widely tunable SG-DBR/EAM transmitters employing a high optical confinement centered MQW (c-MQW) active region fabricated using our simple and robust QWI process [14]. In [13] we propose and demonstrate the proof of concept for a novel QWI and MOCVD regrowth scheme for the integration of low confinement/high saturation power offset MQW (o-MQW) active regions on the same chip as the high optical confinement c-MQW active regions used in the SG-DBR/EAM transmitters. In this work, we expand on the integration scheme with the design and demonstration of UTC type photodiodes realized on the same chip as both high optical confinement c-MQWs for use in high gain lasers or high gain SOA sections, low optical confinement o-MQWs for use in high saturation power SOA sections, and intermixed c-MQW sections for low loss passive waveguides. With the successful placement of these three unique waveguide architectures on a

TABLE I
EPTIAXIAL STRUCTURE EMPLOYED IN UTC REGION (Absorber thickness = WA, Collector thickness = WC)

Layer	*Material*	*Thick (nm)*	*Doping (cm^{-3})*	*Function*
1.	InGaAs:Zn	100	5E19	p-Contact Layer
2.	InP:Zn	1700	5E17-1E18	p-Clad
3.	InGaAs:Zn	WA	2E18	Absorber
4.	InGaAs	8	NID	Cond. Band Smooth
5.	1.24Q	16	NID	Cond. Band Smooth
6.	InP	6	NID	Cond. Band Smooth
7.	InP:Si	7	1E18	Cond. Band Smooth
8.	InP	WC	NID	Collector
9.	InP:Si	30	1E18	Subcollector
10.	1.3Q:Si	15	2E17	Etch Stop
11.	InP:Si	25	8E16	Regrowth Layer
12.	1.3Q:Si	105	5E16	Waveguide
13.	QWI cMQW	153	NID	Waveguide
14.	1.3Q:Si	105	1E17	Waveguide
15.	InP:Si	2000	1E18	n-Clad

single chip and since the definition of widely tunable lasers and QW EAMs only requires the addition of two processing steps to define mirror gratings and an intermediate EAM band-edge, the QWI/MOCVD based processing/growth scheme is completely suited UTC photodiode integration with the previously reported high performance SG-DBR/EAM transmitters. Here we focus on UTC type photodiodes fabricated on top of intermixed QWs, which exhibited high quantum efficiency, excellent photocurrent handling capabilities, minimal response roll-off over the 20 GHz of our testing capability, and open eye diagrams at 40 Gb/s.

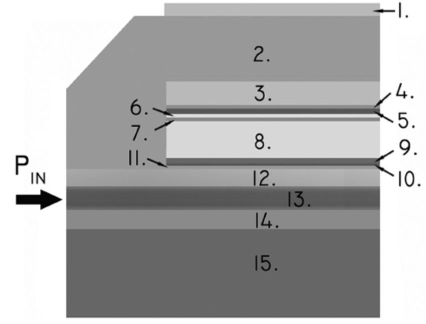

Fig. 1. Side view schematic of UTC structure grown above intermixed QWs.

II. PHOTODIODE DESIGN

By using QWI to render the as-grown base structure QWs transparent, performing an MOCVD regrowth of the appropriate photodiode epitaxial structure, and then using wet chemical selective etching, we demonstrate the first photodetectors fabricated on top of QWI material. The benefits of this photodiode structure over the alternative of using the as-grown c-MQW stack as a p-i-n photodiode are three-fold. First, the use of QWs, which act as potential barriers and hinder carrier escape, can be avoided in the absorber region. Second, since the waveguide core composed of intermixed QWs is set below the absorbing region of the UTC, the absorption profile along the photodiode can be carefully controlled through the choice of collector and absorber layer thicknesses for maximized photocarrier generation uniformity. Finally, since the regrowth of the detector structure is independent of all other components, there are no design constraints on the choice of internal layer structure. With this flexibility, we employ a UTC photodiode structure for its established superior photocurrent handling capabilities [3], [4], [15]. By avoiding the classic space charge saturation effects that plague p-i-n photodiodes, higher saturation current densities are possible allowing for smaller diode areas and hence higher bandwidths. Furthermore, the processing and growth sequence for the integrated UTC structure offers no further difficulty over that of an integrated p-i-n structure, indicating no increase in manufacturing costs.

The epitaxial structure employed in the UTC portion of the device is shown in Fig. 1 with the corresponding layer specifications presented in Table I. The structure was based on that presented in [15] by Ishibashi *et al.* with a few modifications necessary to accommodate our integration scheme. The active layers of the UTC are the neutral InGaAs:Zn absorption layer (#3) and the depleted wide bandgap InP electron collection layer (#8). Under normal operation of the photodiode, carriers are photogenerated in the absorber layer. The minority carriers, electrons, diffuse toward the collector layer where they accelerate to their overshoot velocity and drift across the collector layer. The escape time of the majority carriers, holes, from the absorption layer is negligible since it is set by their dielectric relaxation time [3]. Thus, the carrier transport properties are governed solely by electron transport and the classic space charge effect associated with p-i-n photodiodes is avoided.

The nonbiased band diagram for our proposed structure was simulated with SimWindows software and is shown in Fig. 2. Layers 4–7 function to smooth conduction band discontinuities at the heterointerface and remove potential barriers that could impede electron transport as described in [15]. The most notable differences in our structure compared to that of [15] are the upper p-InP clad (#2), the 1.3Q:Si stop etch (#10), and the intermixed c-MQW region below (#12–14). The use of p-InP cladding above the absorber has been previously employed with no reported performance degradation resulting from hindered carrier transport [4]. The conduction band discontinuities imposed by the 1.3Q:Si stop etch layer between the InP:Si subcollector and InP:Si regrowth layer should not impede the carrier transport properties since at this position electrons should be

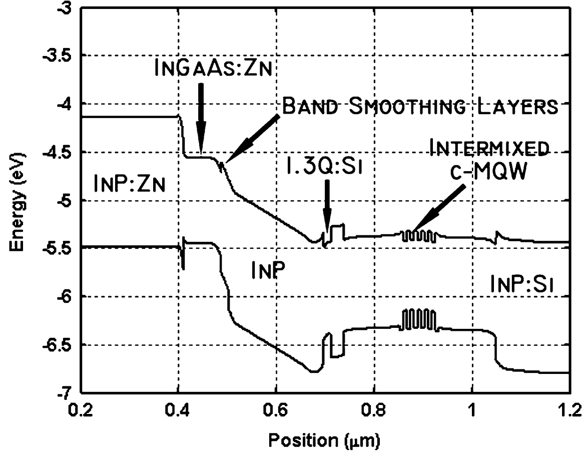

Fig. 2. Simulated 0-V band diagram for our proposed integrated UTC structure.

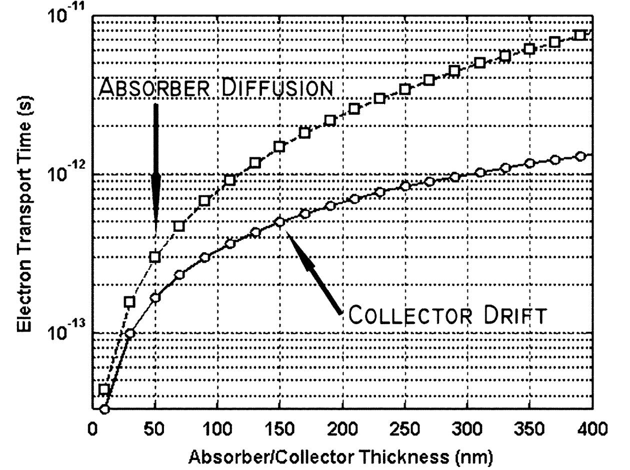

Fig. 3. Calculated electron transport time across collector (circles) and absorber (squares) using (1) and (2), an electron diffusivity of 86 cm^2/s, and carrier velocities given in [3].

collected and governed by majority carrier transport. The thick (1.7 μm) p-cladding and the intermixed active region present in our UTC structure are necessary for the high functionality integration scheme and are expected to result in a somewhat higher series resistance compared to widely reported discrete UTC photodiodes.

III. Photodiode Optimization

In the proposed integrated UTC photodiode structure we must consider the effects imposed by the thickness of the absorber and collector regions on the quantum efficiency, bandwidth, and photocurrent handling capabilities. As discussed above, the total carrier transport time in a UTC photodiode is comprised of two components. Electron drift across the collector and electron diffusion across the absorber. Using the theory outlined in [3], the drift dependent electron transport time from the collector region of the UTC photodiode can be given by (1) and the diffusion time across the absorber by (2). In these expressions, W_C is the collector thickness, W_A is the absorber thickness, $V_e^{\rm os}$ is the electron over shoot velocity in InP, $V_{\rm th}$ is the thermionic emission velocity of electrons in InGaAs, and D_e is the electron diffusivity of electrons in p-InGaAs. Using carrier velocities given in [3] and an electron diffusivity of 86 cm^2/s extracted in [16], we plot the calculated transport times for electrons across the absorber and collector for various layer thicknesses in Fig. 3. As can be seen in the figure, for absorber layer thicknesses greater than 100 nm, the diffusion transport time will dominate the total transport time for reasonable collector thickness of over 100 nm

$$\tau_C = W_C / V_e^{\rm os} \quad (1)$$
$$\tau_A = W_A^2 / 3D_e + W_A / V_{\rm th}. \quad (2)$$

One key benefit to waveguide photodiodes is that the internal quantum efficiency can be much higher than in typical surface illuminated photodiodes [17]. This is easily explained by the differences in the absorption path for the two photodiode geometries. The total detector absorption can be approximated by an exponential decay governed by the product of the material absorption coefficient (α), the optical confinement (Γ) in the absorber layer, and the dimension (L) of the absorption layer normal to optical incidence. In a conventional waveguide photodiode, optical absorption occurs parallel to the growth plane, such that the absorption length (L) is set by the length of the photodiode, which is usually on the order of tens of microns. In a surface illuminated device, absorption occurs normal to the growth direction such that the absorption length (L) is set by the absorber layer thickness, which is usually on the order of 200–500 nm. Although Γ can be close to unity in a surface normal device compared to typical values of 0.1–0.4 for a waveguide device, the extreme contrast in absorption lengths results in higher internal quantum efficiencies for a waveguide photodiode. Using $\alpha = 6800$ cm^{-1} for InGaAs at a wavelength of 1550 nm, $L = 500$ nm and $\Lambda = 1$ for a surface-normal photodiode, the internal efficiency of the device is estimated at 29%. However, for a waveguide photodiode, if we assume an identical absorption coefficient, $L = 25$ μm, and $\Gamma = 0.2$, an internal efficiency of 96% is estimated. With this flexibility in our waveguide photodiode, we choose an absorber thickness of 50 nm such that the electron diffusion component of the carrier transport time is expected to be less than the drift time for collector thicknesses greater than 100 nm as shown in Fig. 3.

In order to study the absorption characteristics, photocurrent generation, and internal quantum efficiency characteristics of the photodiodes, beam propagation simulations were performed using commercially available software from RSoft. The simulations were performed by exciting the fundamental mode of the passive sections comprised of an intermixed c-MQW waveguide. The mode was propagated through a short 5-μm section of lossless passive waveguide before entering the detector region such that the theoretical internal quantum efficiency could be computed most accurately. The simulated absorption profile for our integrated UTC structure with varying collector thicknesses along with that expected in a p-i-n detector formed from the as-grown c-MQW stack consisting of ten 6.5-nm wells is shown in Fig. 4. The loss values of 6800 cm^{-1} used for the InGaAs:Zn and 5000 cm^{-1} used for the p-i-n QWs was extracted experimentally with photocurrent spectroscopy. The three collector thicknesses used in the simulation were 150 (squares), 200 (triangles), and 250 nm (circles) with an absorber thickness

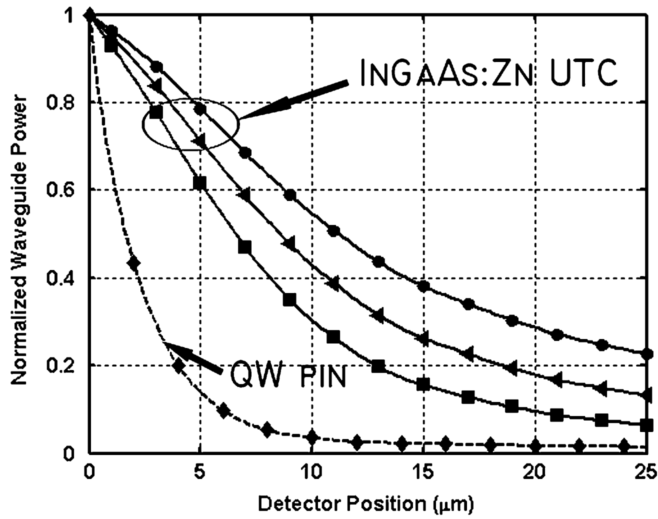

Fig. 4. Simulated waveguide power along photodetector for a QW p-i-n (dashed line) and UTC photodiodes (solid lines). The simulations use a 50-nm-thick absorber and collector thicknesses of 100 (squares), 150 (triangles), and 200 nm (circles).

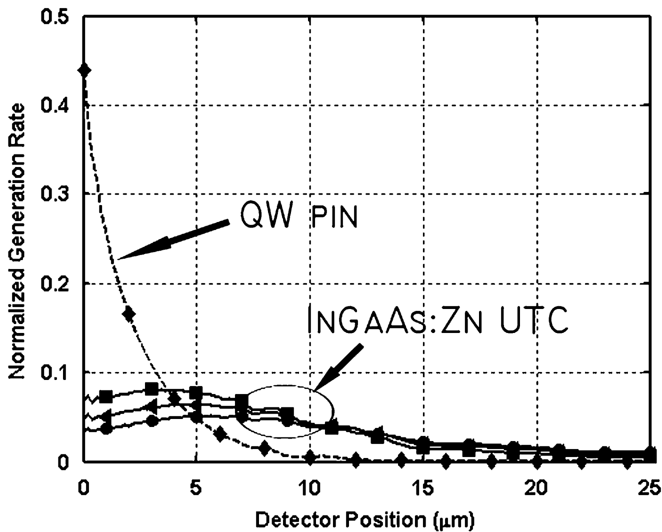

Fig. 5. Simulated generation rate along detector for a QW p-i-n (dashed line) and UTC photodiode (solid lines). The simulations use a 50 nm thick absorber and collector thicknesses of 100 (squares), 150 (triangles), and 200 nm (circles).

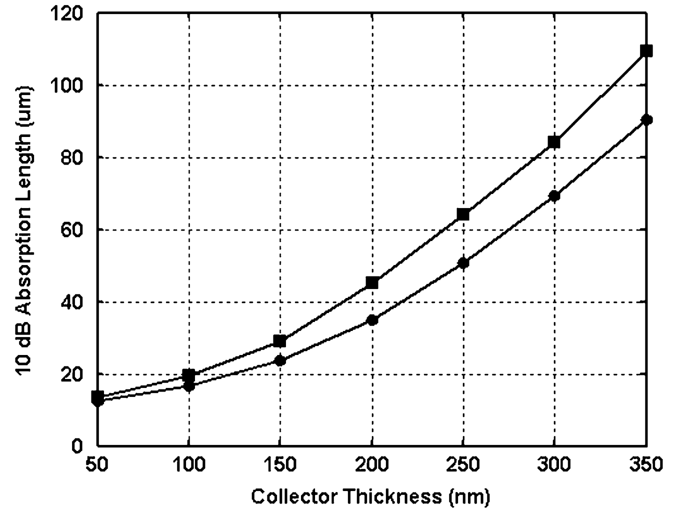

Fig. 6. Simulated 10-dB absorption length versus collector thickness for photodiodes with absorber region thicknesses of 50 (squares) and 100 nm (circles).

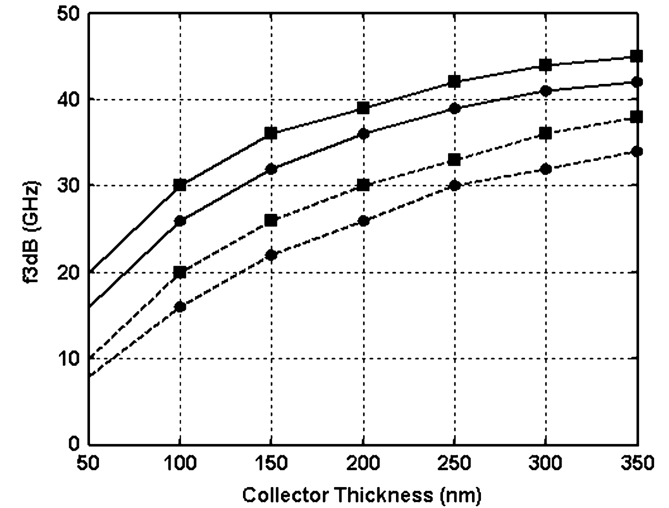

Fig. 7. Simulated *RC* limited 3-dB bandwidth of UTC photodiodes with lengths of 25 (solid lines) and 50 μm (dashed lines) for series resistance values of 30 (squares) and 40 Ω (circles) and effective termination of 25 Ω.

of 50 nm. As shown in Fig. 4, with proper design the absorption profile can be tuned in the UTC device to take on a more linear shape opposed to the fixed steep exponential profile exhibited by the QW-p-i-n. This feature of the integrated UTC structure enables the control over the generation profile since this profile is governed by the slope of the absorption profile. The normalized generation rates along the detector lengths resulting from the absorption profiles are shown in Fig. 4. The UTC type detectors demonstrate a radically more uniform generation rate along the length of the device than does the c-MQW p-i-n detector, with an $\sim$8$\times$ reduction in front end photocurrent generation. This implies that the front-end saturation characteristics plaguing traditional waveguide photodiodes can be avoided using the regrowth scheme.

In Fig. 5 it is clear that the generation rate in the UTC is significantly influenced by the collector thickness, which implies an effect on the device quantum efficiency. Since the collector thickness is inversely proportional to the junction capacitance of the device, the tradeoff between projected internal quantum efficiency and 3-dB bandwidth should be characterized. Fig. 6 plots the simulated 10-dB absorption length versus collector thickness for absorber thicknesses of 50 and 100 nm. From this figure, it is apparent that for collector thicknesses over 150 nm, the diode length required for 90% internal quantum efficiency begins to rapidly increase.

The projected *RC*-limited 3-dB bandwidth versus collector thickness is shown for both the 25-μm-long (solid lines) and 50-μm-long (dashed lines) photodiodes in Fig. 7. Based on the projected absorber/collector carrier transport times shown in Fig. 3, parasitics are expected to limit the bandwidth as the devices in this work were fabricated on conducting substrates. The simulations were performed for series resistance values of 30 and 40 Ω, a pad capacitance of 53 fF, a wire bond inductance of 0.3 nH, and an effective load resistance of 25 Ω. Fig. 6 shows

that a 45-GHz 3-dB bandwidth is possible for a 25-μm long device with a series resistance of 30 Ω. For all curves of Fig. 7, the slope decreases with higher collector thicknesses as the junction capacitance becomes less significant compared to the pad capacitance. In this work we employ a collector thickness of 150 nm in attempt to achieve an internal quantum efficiency of 90% in the 25-μm-long photodiodes. From Fig. 7, a 3-dB bandwidth in the vicinity of 33–36 GHz can be expected with this collector thickness.

IV. Fabrication

The epitaxial base structure is grown on a conducting InP substrate using a Thomas Swan Scientific Equipment Ltd. horizontal-flow rotating-disc MOCVD reactor. The active region consists of ten 6.5-nm compressively strained (1.0%) QWs, separated by 8.0-nm tensile strained (0.3%) barriers, centered within two InGaAsP:Si (1.3Q:Si) layers designed to maximize the optical confinement in the QWs. Following the active region, a 15-nm InP:Si regrowth layer, a 20-nm 1.3Q:Si stop etch, and a 450-nm InP implant buffer layer is grown.

The sample is patterned with Si_xN_y and selectively implanted with P^+ for intermixing. Following the implant, the samples are subjected to our QWI process as described in detail in [12]. In the QWI process, the as grown c-MQWs are shifted in peak photoluminescence wavelength from 1530 to 1410 nm in regions where passive waveguide, low optical confinement QW active regions, or UTC type detectors are desired. Following the QWI process, the implant buffer layer and 1.3Q stop etch layers are removed using selective wet chemical etching, leaving a thin InP:Si regrowth layer on the surface. An MOCVD regrowth is then performed beginning with a 1.3Q:Si stop etch layer, followed by a InP:Si optical confinement tuning layer, an o-MQW active region, and finally a thin InP:Zn cap. The wafer was patterned and a wet chemical etch process was carried such that the o-MQW remained only in regions where low confinement active regions are desired. The sample is then subjected to a second MOCVD step in which the appropriate UTC structure listed in Table I is grown. Following the regrowth, the sample is patterned with Si_xN_y and a selective wet chemical etch process is carried out such that the UTC structure remains in regions where it is desired with the blue-shifted c-MQW below. A final MOCVD regrowth process is performed to grow p-type InP:Zn cladding and p-contact InGaAs:Zn layers. A thorough investigation of the regrowth issues associated with this scheme and with the matter of achieving good material on a surface subjected to QWI can be found in [13].

Following the growth of the p-cladding, surface ridge waveguides were defined. The input waveguide consisted of a 250-μm curved/flared section for reduction of parasitic reflections. A 3.5-μm-thick layer of photo-benzocyclobutene (BCB) was patterned such that it would remain underneath the p-contacts, vias were opened, and p-metal was deposited. A proton implant was performed to provide electrical isolation between electrodes. The wafers were thinned and back-side n-metal was deposited. The die were separated into 3 $\times$ 25 μm^2 and 3 $\times$ 50 μm^2 diodes, soldered to aluminum nitride carriers, and wire bonded (Fig. 2) to a matched load of 50 Ω on a coplanar transmission line to yield an effective termination load of 25 Ω for RF characterization. Scanning electron micrographs of the device cross section and the finished device soldered to the carrier are shown in Fig. 8(a) and (b), respectively.

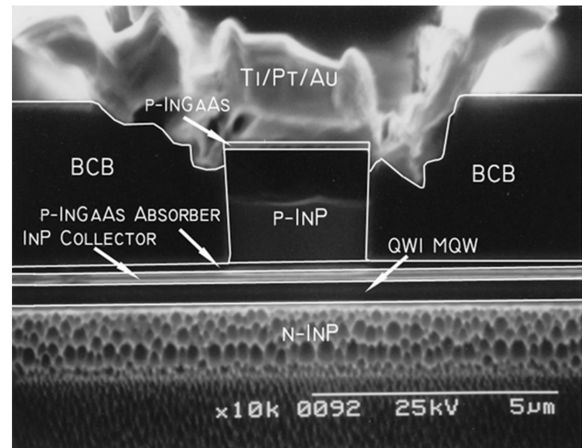

(a)

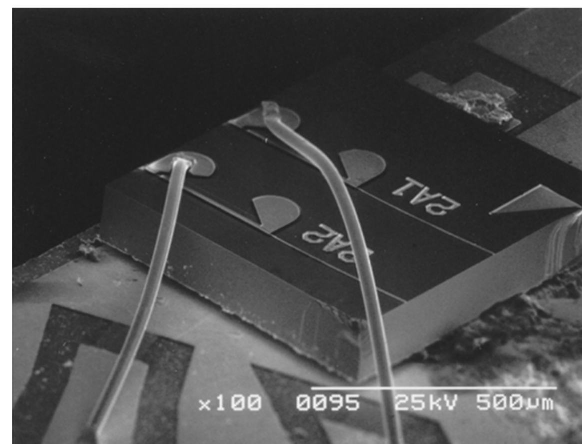

(b)

Fig. 8. Scanning electron micrographs of (a) the cross section of a UTC photodiode, and (b) a device mounted on a AlN carrier for RF testing. Note that the particular device in (b) does not possess the curve/flare input waveguide.

V. Experiment, Results, and Discussion

The passive waveguide loss on the chip was extracted using Fabry–Perot active-passive lasers and found to be $<6\ cm^{-1}$. The internal quantum efficiency of the detectors was estimated by separately reverse biasing two photodetectors configured optically in series. The first detector in the pair is the 25- or 50-μm-long detector in question. The second detector is significantly longer at 250 μm such that essentially all optical power escaping the first detector is absorbed. A 1550-nm continuous-wave (CW) optical input is then applied to the facet through a lensed fiber. The internal quantum efficiency is estimated by taking the fraction of photocurrent detected in the first detector over the sum of photocurrents in both detectors. The estimated internal quantum efficiency for both 25 μm (solid lines) and 50-μm-long (dashed lines) UTC type detectors at reverse biases of 1–4 V is shown in Fig. 9. As can be seen from the figure, the internal quantum efficiency of the 25-μm-long detector is

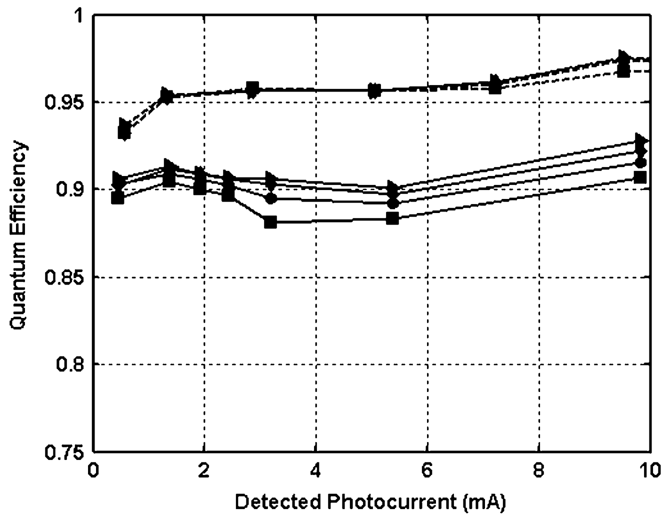

Fig. 9. Measured internal quantum efficiency for a 25 (solid lines) and 50-μm-long (dashed lines) UTC photodiodes under reverse biases of -1 V (squares), -2 V (circles), -3 V (diamonds), and -4 V (triangles).

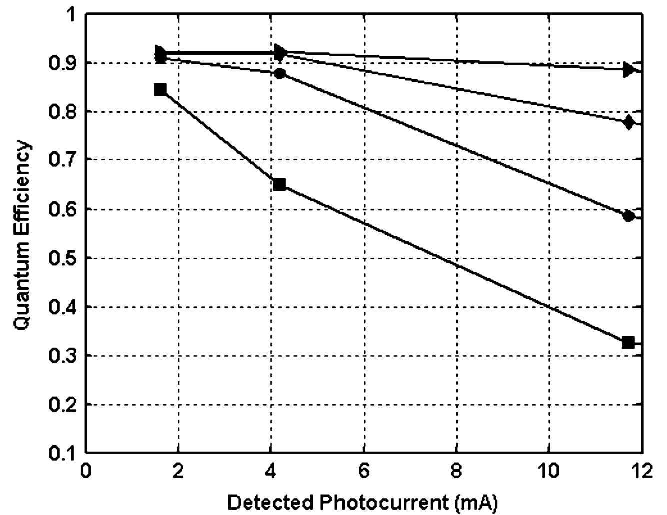

Fig. 10. Measured quantum efficiency for a 75 μm long QW p-i-n under reverse biases of -1 (squares), -2 (circles), -3 (diamonds), and -4 V (triangles).

$\sim$90% as predicted by the beam propagation simulations. The 50-μm-long detector achieves over 95% quantum efficiency. The CW responsivity was measured to be 0.20 and 0.25 A/W at a wavelength of 1550 nm for the 25- and 50-μm-long detectors, respectively. The efficiency values reported here are on the same order as those previously reported for high efficiency discrete waveguide type UTC photodiodes with an external quantum efficiency of 32% [17], however are significantly lower than the 1.14 A/W reported in [5]. With an optimized input waveguide design, a better choice of lensed fiber, and the application of an antireflective coating, the high coupling loss measured at $\sim$6 dB could be significantly reduced, resulting in an increased responsivity.

For direct comparison of the UTC photodiodes realized with the regrowth step to the QW p-i-n detectors we were previously forced to employ in high functionality PICs, QW p-i-n detectors were fabricated on the same chip. Fig. 10 shows the measured efficiency from a 75-μm-long QW p-i-n consisting of ten centered 6.5-nm-thick wells, for a total absorber thickness of 65 nm. As can be seen in the figure, the QW p-i-n detector requires a large bias of -4 V to maintain a linear internal quantum efficiency at the low power levels that these measurements were made. The decrease in quantum efficiency with increasing power at lower bias levels is indicative of space charge saturation occurring in the QW p-i-n detectors. The superior dc saturation performance demonstrated by the UTC photodiodes over the QW p-i-n detectors fabricated on the same chip further reinforces the necessity of integrating the UTC photodiode into high functionality PICs. This fabrication scheme allows the laser and EAM sections to utilize the c-MQW structure while increasing the detector performance by moving from a QW p-i-n to a UTC design [9].

A set of current versus voltage (I–V) sweeps were taken from -5 to $+1.5$ V for the photodiodes at various levels of input power. The dark current generated in a 25-μm-long devices was found to be 0.5 μA at -1 V, 3 μA at -3 V, and 10 μA at -5 V. The reverse bias series resistance for this device was estimated to be 35–40 Ω by taking the slope of an appropriately placed load line through the set of IV curves taken at various input power levels. The series resistance is over 2$\times$ higher than that of high performance discrete photodiodes reported in [2] with similar diode areas. This excess resistance is likely due in part to the $\sim$2$\times$ thicker p-cladding and intermixed c-MQW in our structure, which are necessary for the other waveguide architectures integrated with the photodiode.

The frequency response of the photodiodes was characterized using a 20-GHz Agilent Lightwave Component Analyzer (LCA). The optical signal from the LCA was fed through an erbium-doped fiber amplifier (EDFA) and then coupled into the photodiode waveguide using a lensed fiber. The AlN carrier possessing a matched 50-Ω load was probed with ground-signal-ground probes to extract the electrical signal from the photodiode with an effective termination load of 25 Ω. The frequency response of the photodiode was then characterized as a function of average detected photocurrent and reverse bias.

The optical to electrical response of a 25-μm-long photodiode is shown for various average detected photocurrent levels at a reverse bias of 3 V in Fig. 11. The response curves are normalized to the 5-mA curve such that they are easily differentiated. As can be seen in the figure, the 20-GHz response demonstrates under 0.5 dB of roll-off with average photocurrents up to 20 mA. At an average photocurrent of 25 mA, the roll off is somewhat increased to 0.75 dB and at 35 mA, the 20-GHz roll-off is increased to slightly over 2 dB. When increasing the reverse bias to 4 V at an average photocurrent of 35 mA, the roll-off is decreased to below 1 dB. In Fig. 12 we show the effects of reverse bias on the bandwidth of the same detector at an average photocurrent level of 10 mA. At a reverse bias of 1 V, the 3 dB bandwidth of the 25 μm long photodiode is 16.5 GHz. Upon increasing the bias to -2 V, the bandwidth increases such that there is only 0.5 dB roll-off out to 20 GHz. For reverse biases of 3 and 4 V, there is no roll-off in the response out to 20 GHz.

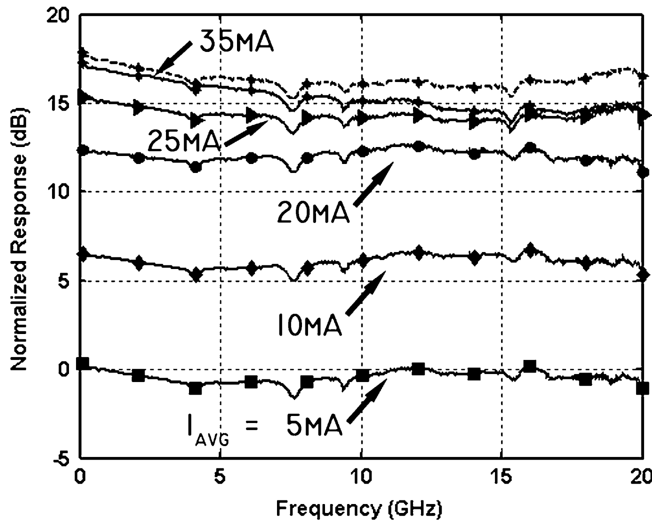

Fig. 11. Optical to electrical response of a 25-μm-long detector for average photocurrents of 5 (squares), 10 (diamonds), 20 (circles), 25 (triangles), and 35 mA (stars) with a 3 V reverse and 35 mA at a −4 V reverse bias (dashed line). Response is normalized to 5 mA data set. Markers represent every 80th data point.

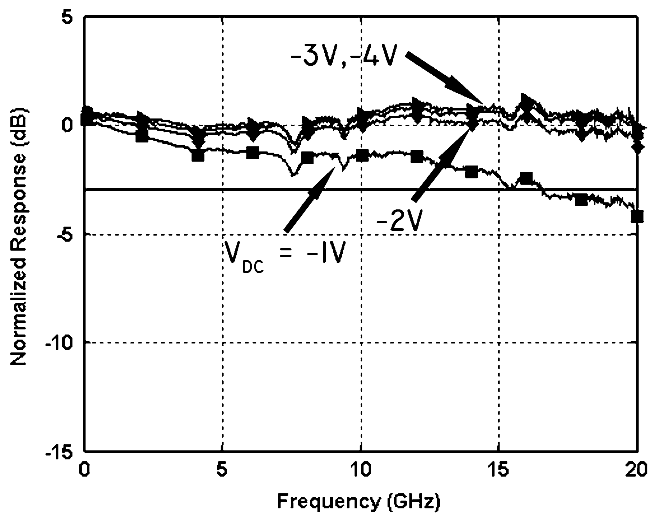

Fig. 12. Optical to electrical response of a 25-μm-long detector for reverse biases of −1 (squares), −2 (diamonds), −3 (circles), and −4 V (triangles) with an average photocurrent of 10 mA. Markers represent every 80th data point.

The optical to electrical response of a 50-μm-long photodiode is presented for various average photocurrent levels at a reverse bias of 4 V in Fig. 13. The response curves are normalized to the 20 mA curve such that they are easily differentiated. As shown in the figure, for average photocurrent levels of up to 40 mA, the roll-off at 20 GHz is under 2 dB, and at 50 mA, the roll-off at 20 GHz is 2.2 dB. The 20-GHz 3 dB photocurrent level was found to be 55 mA. Beyond this photocurrent level, the photodiode demonstrated a marked decrease in quantum efficiency due to saturation effects.

The minimal roll-off of under 0.5 dB demonstrated by the 25-μm-long photodiode and under 2.0 dB demonstrated by the 50-μm-long photodiode out to 20 GHz is in excellent agreement with our response simulations used in Fig. 7, which predicts a 3-dB bandwidth of 33–36 GHz for the 25-μm-long photodiode. The maximum 3-dB bandwidths reported in this initial

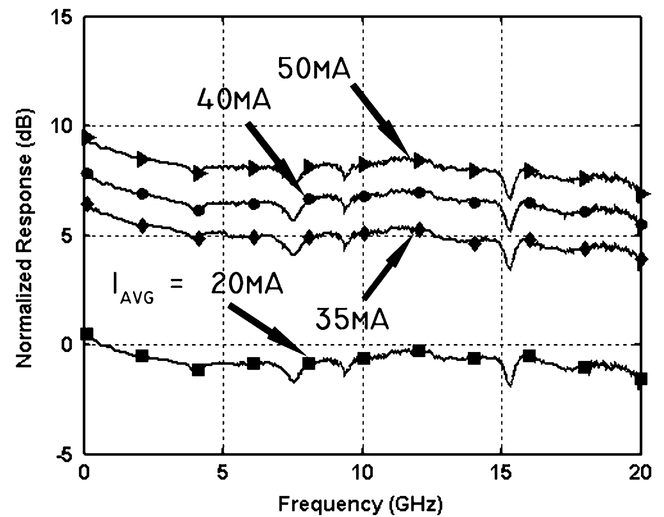

Fig. 13. Optical to electrical response of a 50-μm-long detector for average photocurrents of 20 (squares), 35 (diamonds), 40 (circles), and 50 mA (triangles) with a 4 V reverse bias). Response is normalized to 20 mA data set. Markers represent every 80th data point.

demonstration of UTC photodiodes fabricated using the integration scheme do not reach the >40-GHz levels reported for discrete waveguide type UTC photodiodes. However the reported discrete photodiodes employ semi-insulating substrates for lowered capacitance and have specially designed RF pads for low capacitance and impedance matching [5], [17]. These measures can be easily implemented into the UTC photodiodes reported here in order to greatly improve the response characteristics.

The key performance characteristic offered by the UTC photodiode over p-i-n photodiodes is the improved photocurrent handling capabilities. It can be difficult to directly compare the photocurrent handling capabilities of various detectors reported in literature due to the differences in measurement techniques. However, a special type of p-i-n photodiode to maximize bandwidth and efficiency is reported in [18] and uses similar metrics to characterize the photocurrent handling capabilities. In this report a 90-μm^2 photodiode demonstrates a 50-GHz 3-dB bandwidth at a bias of −3 V under low photocurrent operation. However, upon increasing the photocurrent to 18 mA, the bandwidth falls to under 10 GHz. Since the 75 μm^2 photodiodes reported here operating at the same bias demonstrated no bandwidth degradation up to 25 mA of average photocurrent and still maintained >20 GHz bandwidth for 35 mA of average photocurrent, the advantages offered by the UTC structure are apparent. In [5], state-of-the-art waveguide-type UTC photodiodes with a diode area of 320 μm^2 are characterized by measuring the 3-dB bandwidth at different photocurrent levels and different bias levels. At a bias level of −3 V, the 3-dB bandwidth is maintained in the 22–26-GHz range for photocurrent levels up to 30 mA. This photocurrent handling performance appears to be well inline with the performance reported here for photodiodes of 75 and 150 μm^2 operating at the same bias levels.

To examine the large signal characteristics of the photodiodes, eye diagrams were taken at 10 and 40 Gb/s in a nonreturn to zero (NRZ) format. In the test setup, a CW light source at 1548 nm was modulated using a pattern generator operating with a pseudo-random bit sequence (PRBS) of $2^{31} - 1$. The

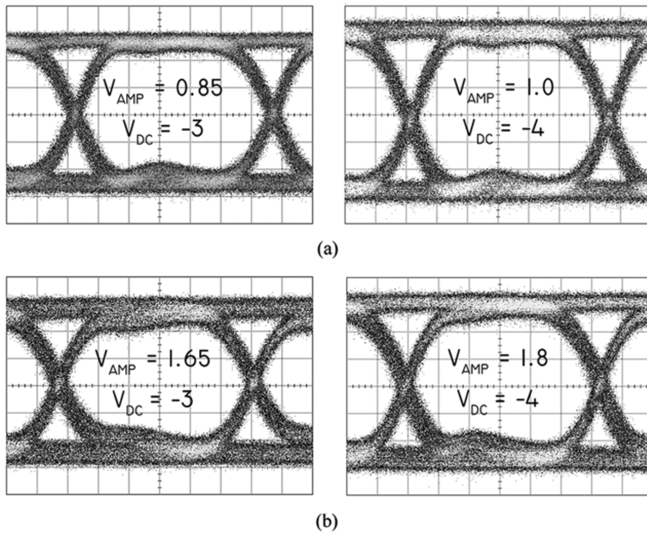

Fig. 14. 10 Gb/s eye diagrams from a (a) 3 × 25 μm^2 and (b) 3 × 50 μm^2 photodiode.

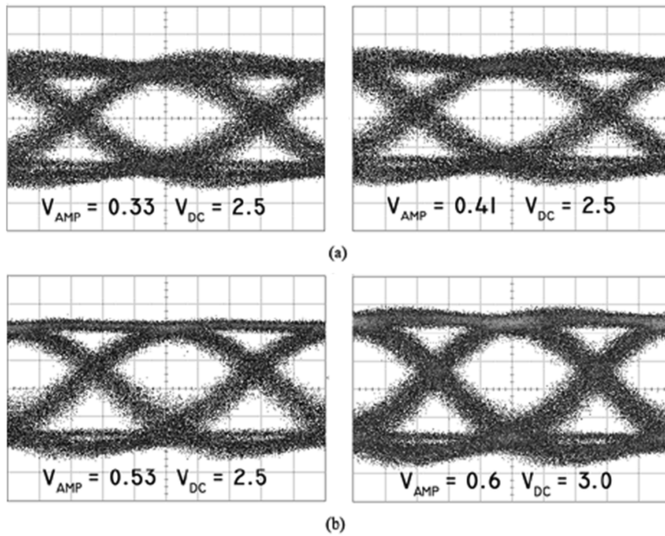

Fig. 15. 40 Gb/s eye diagrams from a 3 × 25 μm^2 μm photodiode.

modulated light was then fed through an EDFA and into the waveguide of the photodiode using a lensed fiber. The electrical output of the device was analyzed using an Agilent DCA.

In Fig. 14(a), we present 10 Gb/s eye diagrams taken from a 25-μm-long detector at a given input power. The voltage amplitude provided by the photodiode at a reverse bias of 3 V, was 0.85 V and at a reverse bias of −4 V, it was 1.0 V. These amplitudes are indicative of minimum peak currents of 34 and 40 mA, respectively, since the voltage drop was obtained over an effective load 25 Ω due to the 50-Ω matching load on the carrier. In Fig. 13(b), eye diagrams from a 50-μm-long detector are shown for a given input power. The voltage amplitude provided by this photodiode at a reverse bias of 3 V was 1.65 V and at a reverse bias of 4 V it was 1.8 V. These amplitudes are indicative of minimum peak photocurrents of 66 and 72 mA, respectively.

In Fig. 15(a), we present 40 Gb/s eye diagrams taken from a 25-μm-long detector with two different input power levels at a reverse bias of 2.5 V. The voltage amplitude of these eyes was measured at 0.33 and 0.41 V. As can be seen from the figure, the eye diagrams are open and demonstrate no difference in shape for the two input power levels. In Fig. 14(b), eye diagrams are shown for a constant input power at reverse biases of 2.5 and 3.0 V. The higher crossing point of the eye diagram driving a voltage amplitude of 0.53 V at a reverse bias of 2.5 V is indicative of the onset of saturation. However, upon increasing the reverse bias to 3.0 V, the voltage amplitude is increased to 0.6 V and the crossing point returns to its normal position. The 0.6 V amplitude provided by the photodiode at 3 V is indicative of a minimum peak current of 24 mA in the photodiode.

VI. Conclusion

We have presented the concept and design for the realization of UTC type photodiodes fabricated using a novel QWI and MOCVD regrowth scheme. The photodiodes were fabricated on the same chip as high-gain c-MQW active regions, low optical confinement o-MQW active regions, and intermixed c-MQW passive waveguide sections. Since this scheme is an extension of and completely compatible with our established SG-DBR/EAM transmitter process, we demonstrate an extremely flexible integration technology to enable the monolithic integration of UTC photodiodes with high gain widely tunable laser diodes, high efficiency EAMs, and high saturation power SOA's.

In this first demonstration of UTC photodiodes fabricated on intermixed QWs, the UTC photodiodes exhibited greatly reduced DC saturation characteristics over the QW p-i-n photodiodes fabricated on the same chip that were previously used as detectors in high functionality PICs. The 3 × 25 μm^2 UTC photodiodes exhibited high internal quantum efficiencies of 90% and a minimal response roll-off out to 20 GHz, which is in good agreement with simulations. No significant degradation in the bandwidth out to 20 GHz was observed for average photocurrent levels up to 25 and 50 mA for the 3 × 25 μm^2 and the 3 × 50 μm^2 photodiodes, respectively. Eye diagrams at 10 Gb/s demonstrated peak photocurrents of 40 and 72 mA in the 3 × 25 μm^2 and 3 by 50 μm^2 photodiodes, respectively. Open 40 Gb/s eye diagrams were achieved with a voltage amplitude of 0.6 V. Future work will include further optimization of the UTCs for increased bandwidth.

References

[1] S. Srivastava and K. P. Roenker, "Numerical modeling study of the InP/InGaAs unitraveling-carrier photodiode," *Solid State Electron.*, vol. 48, pp. 461–470, 2004.

[2] S. Demiguel, L. Giraudet, L. Joulaud, J. Decobert, F. Blache, V. Coupe, F. Jorge, P. Pagnod-Rosiaux, E. Boucherez, and F. Devaux, "Evanescently coupled photodiodes integrating a double stage taper for 40 Gb/s applications—Compared performance with side-illuminated photodiodes," *J. Lightw. Technol.*, vol. 20, no. 12, pp. 2004–2014, Dec. 2002.

[3] T. Ishibashi, T. Furuta, H. Fushimi, and H. Ito, "Photoresponse characteristics of unitraveling-carrier photodiodes," *Proc. SPIE*, vol. 4283, pp. 469–479, 2001.

[4] D. A. Tulchinsky, X. Li, N. Li, S. Demiguel, J. C. Campbell, and K. J. Williams, "High-saturation current wide bandwidth photodetectors," *IEEE J. Sel. Topics Quantum Electron.*, no. 4, pp. 702–708, Jul./Aug. 2004.

[5] J. W. Shi, Y. S. Yu, C. Y. Wu, P. H. Chiu, and C. C. Hong, "High-speed, high-responsivity, and high-power performance of near ballistic unitraveling-carrier photodiode at 1.55 μm wavelength," *IEEE Photon. Technol. Lett.*, vol. 17, no. 9, pp. 1929–1931, Sep. 2005.

[6] T. Yoshimatsu, S. Kodama, K. Yoshino, and H. Ito, "100 Gbit/s error-free retiming operation of monolithic optical gate integrating with photodiode and electroabsorption modulator," *Electron. Lett.*, vol. 40, no. 10, pp. 626–628, 2004.

[7] M. Sysak, J. Barton, L. Johansson, J. Raring, E. Skogen, M. Mašanović, D. Blumenthal, and L. Coldren, "Single chip wavelength conversion using a photocurrent driven (PD) EA modulator integrated with a widely tunable sampled grating DBR (SGDBR) laser," *IEEE Photon. Technol. Lett.*, vol. 16, no. 9, pp. 2093–2095, Sep. 2004.

[8] K. Morito, S. Tanaka, S. Tomabechi, and A. Kuramata, "A broad-band MQW semiconductor optical amplifier with high saturation output power and low noise figure," presented at the *Semicond. Opt. Amp. Applicat. Meeting. PD1-1*, San Francisco, CA, Jun. 30, 2004.

[9] J. Raring, E. Skogen, L. Johansson, M. Sysak, J. Barton, M. L. Mašanović, and L. Coldren, "Quantum well intermixing for monolithic integration: A demonstration of novel widely tunable 10 Gb/s transmitters and wavelength converters," presented at the *Integrated Photonics Research Conf.*, San Francisco, CA, 2004, Paper IWC3.

[10] J. Binsma, P. Thijs, T. VanDongen, E. Jansen, A. Staring, G. VanDenHoven, and L. Tiemeijer, "Characterization of butt-joint InGaAsP waveguides and their application to 1310 nm DBR-type MQW Ganin-clamped semiconductor optical amplifiers," *IEICE Trans. Electron.*, vol. E80-C, pp. 675–681, 1997.

[11] M. Aoki, M. Suzuki, H. Sano, T. Kawano, T. Ido, T. Taniwatari, K. Uomi, and A. Takai, "InGaAs/InGaAsP MQW electroabsorption mofulator integrated with a DFB laser fabricated by bandgap energy control selective area MOCVD," *IEEE J. Quantum Electron.*, vol. 29, no. 6, pp. 2088–2096, Jun. 1993.

[12] E. Skogen, J. Raring, J. Barton, S. DenBaars, and L. Coldren, "Post-growth control of the quantum-well band edge for the monolithic integration of widely tunable lasers and electroabsorption modulators," *IEEE J. Sel. Topics Quantum Electron.*, vol. 9, no. 5, pp. 1183–1190, Sep./Oct. 2003.

[13] J. Raring, E. Skogen, S. Denbaars, and L. Coldren, "A study of regrowth interface and material quality for a novel InP based architecture," *J. Cryst. Growth*, vol. 273, no. 1–2, pp. 26–37, Dec. 2004.

[14] J. Raring, E. Skogen, L. Johansson, M. Sysak, S. Denbaars, and L. Coldren, "Widely tunable negative-chirp SG-DBR laser/EA-modulated transmitter," *J. Lightw. Technol.*, vol. 23, no. 1, p. 80–86, Jan. 2005.

[15] T. Ishibashi, T. Furuta, H. Fushimi, S. Kodama, H. Ito, T. Nagatsuma, N. Shimizu, and Y. Miyamoto, "InP/InGaAs unitraveling-carrier photodiodes," *IEICE Trans. Elelctron.*, vol. E83-C, no. 6, Jun. 2000.

[16] N. Shimizu, N. Watanabe, T. Furuta, and T. Ishibashi, "Electron diffusivity in p-InGaAs determined from the pulse response of InP/InGaAs unitraveling-carrier photodiodes," *Appl. Phys. Lett.*, vol. 76, no. 9, pp. 1191–1193, Feb. 2000.

[17] Y. Muramoto, K. Kato, M. Mitsuhara, O. Nakajima, Y. Matsuoka, N. Shimizu, and T. Ishibashi, "High-output, high speed, high efficiency unitraveling-carrierwaveguide photodiode," *IEE Electron. Lett.*, vol. 34, no. 1, pp. 122–123, 1998.

[18] Y. Muramoto and T. Ishibashi, "InP/InGaAs pin photodiode structure maximizing bandwidth and efficiency," *IEE Electron. Lett.*, vol. 39, no. 24, pp. 1749–1750, 2003.

James W. Raring (S'03) was born in Ramsey, NJ, in 1978. He received the B.S. degree from the Materials Engineering Department, California Polytechnic State University, San Luis Obispo, in 2001. He is currently pursuing the Ph.D. degree in materials science from the University of California, Santa Barbara.

His current research focuses on design, growth, and fabrication of wavelength-agile photonic integrated circuits. His work employs flexible quantum-well intermixing and MOCVD growth schemes for the realization of highly functional active monolithic photonic circuits.

Erik J. Skogen (M'99) was born in Minneapolis, MN, in 1975. He received the B.S. degree from Iowa State University, Ames, in 1997, and the M.S. and Ph.D. degrees from the University of California, Santa Barbara (UCSB), in 1999 and 2003, respectively. His dissertation work involved the development and application of quantum-well intermixing techniques to widely tunable sampled-grating DBR lasers and photonic integrated circuits (PIC).

He was a Postdoctoral Researcher with UCSB where he investigated advanced PICs. In 2005, he joined Sandia National Laboratories, Albuquerque, NM, as a Senior Member of Technical Staff. His current research involves advanced monolithic integration techniques for next generation PICs.

Chad S. Wang (S'99) was born in Racine, WI, in 1979. He received the B.S. degree from The University of Texas at Austin, in 2001, and the M.S. degree from the University of California, Santa Barbara, in 2002, where he is currently working toward the Ph.D. degree in electrical and computer engineering.

His research interests include the development of integrated laser-modulators for optical interconnect applications. He is also involved in molecular beam epitaxy growth of III–V semiconductor vertical-cavity lasers and avalanche photodetectors.

Jonathon S. Barton (M'00) received the B.S. degree in electrical engineering and material science at the University of California, Davis, in 1997. He received the Ph.D. degree in electronic materials from the University of California, Santa Barbara, where he was an Intel Fellow.

Currently, he is an Assistant Project Scientist for the LASOR DARPA grant working on the growth, fabrication, and high-speed testing of many monolithic optoelectronic components such as tunable lasers, modulators, and photocurrent-driven wavelength converters.

Dr. Barton is a member of IEEE LEOS, OSA, and SPIE.

Gordon B. Morrison received the B.A.Sc. (hons.) degree in engineering physics from Simon Fraser University, Vancouver, BC, Canada, in 1997 and the Ph.D. degree in engineering physics from McMaster University, Hamilton, ON, Canada, in 2002.

From 1998 to 2002, he spent more than a year as a Graduate Student Researcher at Nortel Networks, Ottawa, ON. After completing the Ph.D., he spent eight months as a Postdoctoral Researcher at McMaster University. From 2003 to 2005, he was a Visiting Assistant Research Engineer in the Department of Electrical and Computer Engineering, University of California, Santa Barbara. Since June 2005, he has been an Optical Device Engineer at Three Five Photonics BV, Houten, The Netherlands. His interests have included design of integrated laser/EAM modulators using quantum-well intermixing for both GaAs and InP material systems, as well as photocurrent spectroscopy for material characterization and device optimization. Other interests have included modeling the spectra of DFB lasers, and modeling the gain in asymmetric multiple-quantum-well lasers.

Stéphane Demiguel (M'04) was born in Gennevilliers, France, in 1971. He received the engineer degree in electrical engineering from the Ecole Supérieure d'Ingenieurs en Génie Electrique, Rouen, France, in 1996 and the Ph.D. degree in optoelectronic from Rouen University, Rouen, in 2001.

In 2000, he worked on the design and measurements of high-speed photodiodes in Alcatel Opto+, Marcoussis, France. In particular, he was involved in optical and electrical modeling for optoelectronic devices. In 2002, he joined Prof. J. Campbell's group at the University of Texas, Austin. He is currently working on high-speed PIN, APD, and high-power photodiodes utilizing an evanescently coupled approach integrating a multimode waveguide.

Steven P. DenBaars (M'91) is a Professor of Materials and Electrical Engineering at the University of California, Santa Barbara (UCSB). From 1988–1991, he was a Member of the Technical Staff at Hewlett-Packard, involved in the fabrication of high-brightness LEDs. In 1991, he joined the faculty of UCSB, where he is developing new solid-state optoelectronic devices. His research also involves MOCVD growth of GaN- and InP-based tunable lasers and detectors. Currently, he is an Associate Director of the Solid-State Lighting and Display Center (SSLDC) at UCSB, which is developing new, more energy-efficient light sources. Special interests include the effect of materials properties on device performance, blue VCSEL lasers, and microwave power transistors. He has authored over 200 technical publications, three book chapters, 100 conference presentations, and over seven patents.

Dr. DenBaars received a National Science Foundation Young Scientist Award in 1995, and the Young Scientist Award from the International Symposium on Compound Semiconductors in 1998.

Larry A. Coldren (S'67–M'72–SM'77–F'82) received the Ph.D. degree in electrical engineering from Stanford University, CA, in 1972.

After 13 years in the research area at Bell Laboratories, he was appointed Professor of Electrical and Computer Engineering at the University of California at Santa Barbara (UCSB) in 1984. At Bell Labs Coldren initially worked on waveguided surface-acoustic-wave signal processing devices and coupled-resonator filters. He later developed tunable coupled-cavity lasers using novel reactive-ion etching (RIE) technology that he created for the then new InP-based materials. At UCSB he continued work on multiple-section tunable lasers, in 1988 inventing the widely tunable multi-element mirror concept, which is now fundamental to many of Agility's products. During the late eighties he also developed efficient vertical-cavity multiple-quantum-well modulators, which led to novel vertical-cavity surface-emitting laser (VCSEL) designs that provided unparalleled levels of performance. In 1986, he assumed a joint appointment with Materials and Electrical and Computer Engineering and, in 2000, the Fred Kavli Chair in Optoelectronics and Sensors. He is also Chairman and Chief Technology Officer of Agility Communications, Inc. At UCSB, his efforts have included work on novel guided-wave and vertical-cavity modulators and lasers, as well as the underlying materials growth and fabrication technology. He is now investigating the integration of various optoelectronic devices, including optical amplifiers and modulators, tunable lasers, wavelength converters, and surface-emitting lasers. He continues to be active in developing new photonic integrated circuit (PIC) and VCSEL technology, including the underlying materials growth and fabrication techniques. In recent years, for example, he has been involved in the creation of vertical and in-plane GaN-based emitters, efficient all-epitaxial InP-based VCSEL's, and a variety of PICs incorporating numerous optical elements for widely tunable integrated transmitters, receivers, and wavelength converters. He has authored or coauthored more than 700 papers, five book chapters, one textbook, and has been issued 36 patents. He has presented dozens of invited and plenary talks at major conferences.

Prof. Coldren is a Fellow of the Optical Society of America (OSA) and the Institute of Electrical Engineers (IEE), U.K., a Member of the National Academy of Engineering, and the recipient of the 2004 John Tyndall Award, and a member of the National Academy of Engineering.